Detection and analysis of fracture initiation in microelectronic packages using methods of digital speckle correlation and fiber Bragg grating

Hua Lu, Ming Zhou, Xijia Gu
Ryerson University,350 Victoria Street, Toronto, On. M5B 2K3, Canada

Abstract
Onset fracture detection is the key of a novel hybrid approach for the reliability assessment of advanced microelectronics. Focusing on structurally weak yet functionality-wisely critical sites such as the solder and multi-material interconnects, the approach employs some microscopic deformation measurement techniques such as Digital Speckle Correlation and Fiber Bragg Grating sensor. Case applications presented to illustrate the new approach involve a radio frequency power amplifier assembly and a large area array package with 2809 solder joints. In both applications the packages' reliability sensitive sites were identified, followed by mechanical and thermal tests aimed to measure deformation parameters in these sites. Assisted by visual failure inspections, the data analysis pinpointed the temperature/time instant the fracture initiated, which made possible to determine the package's failure critical load or condition.

1. Introduction

The reliability and service life of a microelectronic package are largely dictated by the state and the history of the stress and strain in its dissimilar material interconnects. For most packages, the multi-material interface fracture dominates the cause of the mechanically and thermally induced failure. To identify the fracture and to detect its initiation and progress with a real package can effectively determine the package's failure critical load and critical condition. In the proposed hybrid approach, this is mainly accomplished with the microscopic, quantitative stress/strain measurement technique to enable the failure physics based analysis. This paper introduces the methods of digital speckle correlation and fiber Bragg grating that both have been successfully applied in the study. The two-step approach generally consistes of, the first, a simplified, mechanistics-based analysis to identify package's reliability sensitive sites; and the second, the experiments to test the package for determining the critical condition that causes the package's first fail (or the crack initiation). The critical load once established can be treated as the lower bound of the package's resistance to failure. The new approach is significant since it provides viable alternative to the current statistics-based testing for reliability evaluation, which usually takes a very lengthy and constly process. Furthermore, the knowledge gained in the applications facilitates the understanding of the mechnisms of fracture initiation, and the data obtained contribute to form the failure physics based prediction for the package damage development and the terminal failure.

2. Experimental techniques for microscopic strain measurement

2.1 Method of Digital Speckle Correlation (DSC)

DSC is a computer vision method measuring in-plane deformation of a surface [1]. At an adjustable spatial resolution the method records a series images with one reference and the others deformed images of different states. The image processing involves a pair such images at a time (i.e., the reference and another deformed one), and proceeds point by point on the images. At each point, the processing evaluates the light intensity correlation between a pair of the image subset surrounding the point, and obtains the deformation parameters for the point. The de-correlation between the image subsets is defined by a factor S as

$$S(u,v,\partial u/\partial x,\partial u/\partial y,\partial v/\partial x,\partial v/\partial y)=1-\frac{\sum f(x,y)g(x^*,y^*)}{\sqrt{\sum f^2(x,y)\sum g^2(x^*,y^*)}} \qquad (1)$$

S is a function of six-variables including two in-plane displacement components and four displacement partial derivatives defined at the subset center. $f(x, y)$ and $g(x, y)$ are the subset of digitally recorded images, which ar the discrete functions representing resepectively the light intensity of the reference and the deformed image subset. $g(x^*, y^*)$ is an artificially reconstructed, deformed image subset based on $g(x, y)$. (x, y) is a point located at a regular pixel location of the CCD (charge-coupled device) sensor. Due to the surface deformation, (x, y) moves to a new location (x^*, y^*) which is not usually a pixel location. (x, y) and (x^*, y^*) are related via the law of 2D deformation kinematics as follows:

$$x^*=x+u+\frac{\partial u}{\partial x}\Delta x+\frac{\partial u}{\partial y}\Delta y, \qquad y^*=y+v+\frac{\partial v}{\partial x}\Delta x+\frac{\partial v}{\partial y}\Delta y \qquad (2)$$

whrere Δx and Δy are the local coordinates of the point (x, y) in the subset. With known deformation parameters at (x, y), $g(x^*, y^*)$ is reconstructed via interpolating the pixel readings of the original $g(x, y)$. The deformation parameters or the roots of the S function are unknown at the start, but are solved iteratively with initially estimated unknown parameters. The numerical processing progressively improves the estimates and eventually gives a minimized S, signifying a good correlation reached between $f(x, y)$ and $g(x^*, y^*)$. The six updated variables are thus considered to have converged to their respective true values, and the strains are further obtained based on the measured displacement gradients as

$$\varepsilon_x=\sqrt{1+2\frac{\partial u}{\partial x}+(\frac{\partial u}{\partial x})^2+(\frac{\partial v}{\partial x})^2}-1, \quad \varepsilon_y=\sqrt{1+2\frac{\partial v}{\partial y}+(\frac{\partial v}{\partial y})^2+(\frac{\partial u}{\partial y})^2}-1, \quad \gamma_{xy}=\arcsin\frac{\frac{\partial u}{\partial y}+\frac{\partial v}{\partial x}+\frac{\partial u}{\partial x}\frac{\partial u}{\partial y}+\frac{\partial v}{\partial x}\frac{\partial v}{\partial y}}{(1+\varepsilon_x)(1+\varepsilon_y)} \qquad (3)$$

No prior knowledge of material properties are required if the temperature is not vaiable, otherwise the measured apparent strains generally consist of mechanical and thermal terms. Yet for a thermally isotropic material, equations (3) becomes:

$$\varepsilon_x=\sqrt{1+2\frac{\partial u}{\partial x}+(\frac{\partial u}{\partial x})^2+(\frac{\partial v}{\partial x})^2}-1+\alpha\cdot\Delta T, \qquad \varepsilon_y=\sqrt{1+2\frac{\partial v}{\partial y}+(\frac{\partial v}{\partial y})^2+(\frac{\partial u}{\partial y})^2}-1+\alpha\cdot\Delta T,$$
$$\gamma_{xy}=\arcsin\frac{\frac{\partial u}{\partial y}+\frac{\partial v}{\partial x}+\frac{\partial u}{\partial x}\frac{\partial u}{\partial y}+\frac{\partial v}{\partial x}\frac{\partial v}{\partial y}}{(1+\varepsilon_x)(1+\varepsilon_y)} \qquad (4)$$

where α is the material's coefficient of linear thermal expansion and ΔT the temperature difference between the reference and deformed states. It is noted that the temperature change has no contribution to the measured apparent shear strain for thermally isotropic materials. The schematics in Fig. 1 shows the hardware system for the DSC technique. Being a light intensity correlation based technique, DSC requires that the object surface possesses variable surface light reflectivity. For surfaces with little natural texture, spry-painting a random pattern of black and white speckles is an effective solution. Given that the six deformation parameters are generated simultaneously and independently regardless their interrelationships, the strain terms are obtained without going through the error prone numerical differentiation of discrete displacement measurements. The measurement accuracies reach submicron for the displacement and 200 με for the strain. The spatial resolution is determined by the optical magnification of the imaging system and the camera pixel resolution, and can reach submicron if the system and environmental stability is carefully managed.

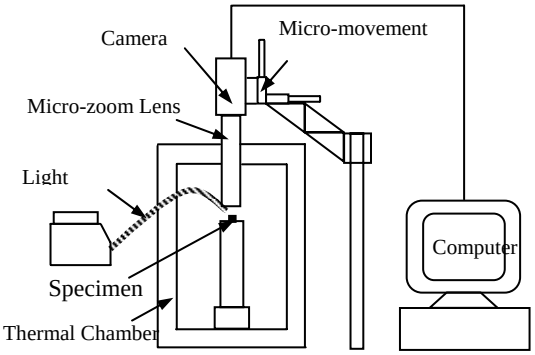

Fig. 1 Schematic diagram showing DSC measurement system.

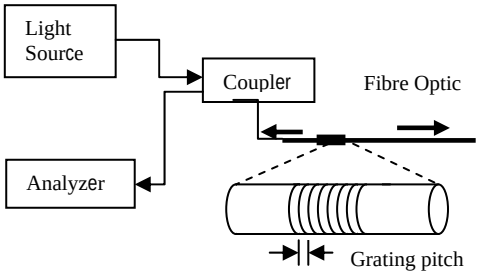

Fig. 2 Schematic showing FBG strain sensor structure and measurement setup.

2.2 Method of fiber Bragg grating (FBG) strain sensor

FBG method uses a phase grating in an optical fiber as the strain sensor, which makes the measurement immune from electromagnetic interferences [2]. The sensing element (the Bragg grating) is photo-inscribed into the core of a silica fiber. The schematic in Fig. 2 shows a broadband light beam propagates along the fiber and hits the grating. Only a portion of the light with a particular wavelength is bounced back from the grating. The wavelength (so-called Bragg wavelength) is determined by the grating pitch. In the strain sensor applications, a laser light is used and the fiber grating is made that its Bragg wavelength matches that of the laser. When the sensor deforms, its grating pitch changes accordingly, inducing a shift of the Bragg wavelength. The amount of the shift is proportional to the sensor's axial strain, as governed by relationship as follows:

$$\Delta\lambda_B = 2\,\mathrm{n}\,\Lambda\left(\left\{1-\left(\frac{\mathrm{n}^2}{2}\right)\left[p_{12}-\nu\left(p_{11}-p_{12}\right)\right]\right\}\varepsilon\right) \qquad (5)$$

where $\Delta\lambda_B$ is the wavelength shift, ε is the applied strain, $p_{i,j}$ is the Pockel's stress-optic coefficients, v is the Poisson's ratio and n is the refractive index of the fiber core. The wavelength shift can be detected using an optical spectrum analyzer. The FBG sensor offers a wide dynamic range and a strain sensitivity of about 2 με. Similar to a single electric resistance strain gauge, a FBG strain sensor responds to the normal strain along its axial direction only. The capability of microscopic strain measurement owes to the fiber's fine diameter (around 10 μm), the short gauge/grating length (down to a fraction of a millimeter) and the sensor's very light weight. A verification test conducted for this study obtained the measurements with a strain gauge and a FBG simultaneously recorded on a cantilever beam, which gave a relative difference of less than 0.5 %.

3. Case studies

3.1 Evaluation of thermal-mechanical reliability of RFPA assembly

RF (radio frequency) PA (power amplifier) is an expensive part in a wireless communication system. The photos in Fig. 3(a) show the prototype of a new board-level assembly. The PCB (printed circuit board) is a ceramic-epoxy laminate and is embedded with a coin structure as a PA carrier and to facilitate the heat dissipation. The embedded coin is connected to the PCB via tab locks of the coin, and the connection is made with a conductive silver-epoxy adhesive.

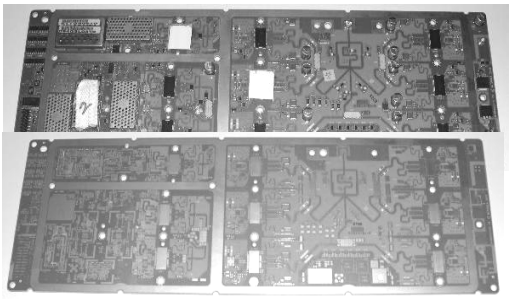

Fig. 3(a) Photos for an assembly board showing PA components (top), and a bare board showing embedded coins (bottom).

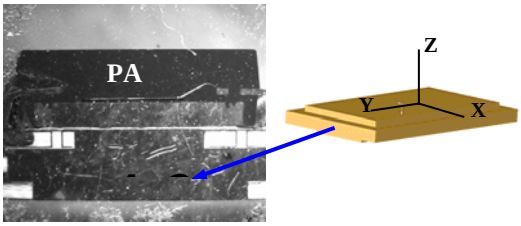

Fig. 3(b) Photo of a cross section of the RFPA assembly showing PA on top and heat sink on bottom of a coin (left); and a three-dimensional drawing showing the coin geometry (right).

The heat sink is bolted to PCB first, and both PA and the heat sink are reflow soldered to the coin on its opposite sides. A thin layer of TIM (thermal interface material) layer is inserted between the coin and the heat sink for better thermal impedance. The mismatch of CTE (coefficient of thermal expansion) between the laminate (44 ppm/^{o}C) and the coin (17 ppm/^{o}C) at the interconnection became an issue of concern. The weight of the coin and the heat sink also attracted the attention since it contributes to bending at the interconnection. As illustrated in Fig. 4, the constraint by the bolts induces additional coupled bending and compression to worsen the stress condition during reflow soldering. The analysis perceived that the interconnect debonding could be a potential mode of failure, and the delamination could damage the nearby copper routings to threat the package's functionality. With the cost and time constraint, a conventional liquid-

to-liquid thermal shock test was conducted on a bare PCB with embedded coins (no PA and heat sink). The test consisted of three-steps: 1000 cycles at -40 to 115 °C, followed by 500 cycles at -40 to 125 °C and 500 cycles with a five-minute dwell at -40 to 150 °C. Failure inspections followed the test found no issue. Yet to continue with a full-scale testing on assembly packages would cost enormously more and consume far longer time. This justified that the further evaluation employs the alternative, analytically-experimentally based approach.

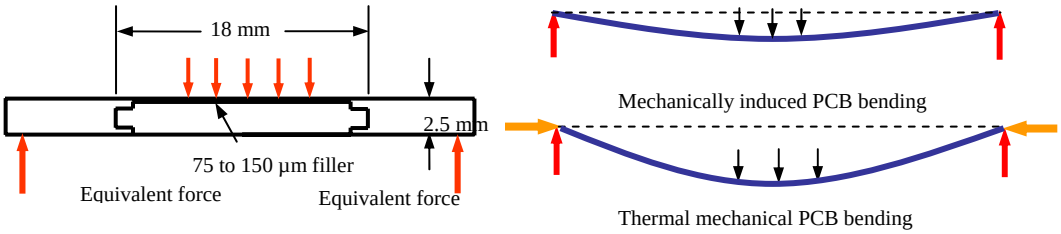

Fig. 4 The sketch of the PCB with embedded coin (left); The weight of the coin structure, the PA and heat sink together adds an effective bending load to PCB (top right); Under elevated temperature, PCB is subject to an additional in-plane force (bottom right).

A simple 2D linear-elastic finite-element (FE) model was constructed with the aim to identify failure sensitive sites. The results as shown in Fig 5 confirmed the shear strain concentration at these sites. Given the guidance, the microscopic deformation measurement focused on the sandwiched area of the prototype. The local areas probed include the vertical adhesive layers joining the tab locks and the PCB, and the solder joints interconnecting the component leads and the PCB copper pads. The experimental setup, as Fig. 6 shows, is composed of the imaging system, the thermal chamber and the sample fixture.

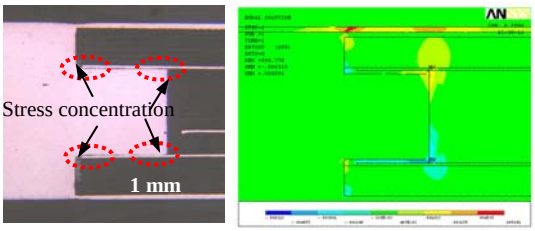

(a) **(b)**

Fig. 5 (a): tab-lock and PCB multi-material interfaces; (b): shear strain obtained by FEA.

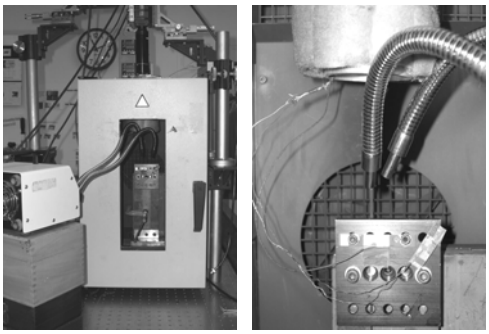

Fig. 6 Experimental setup for thermal-mechanical strain measurement (left); close-up view of a test sample, light source and camera lens.

The types of the tested samples include the bare PCB, the PCB with heat sink, and the assembly with both RF and heat sink. Fig. 7 shows a sketch of the assembly unit. The TIM foils had two different thicknesses of 3-mil (0.075 mm) and 6-mil (0.150 mm). The strain due to the heat sink installation is referred to as the

mechanical strain, and that induced by the temperature change as the thermal-mechanical strain. With the magnification of 1.21 μm/pixel, these quantities were measured: 1) the thermal-mechanical strains at the interfaces in bare PCB; 2) mechanical strain in the PCB with heat sink installed at 10 lb-in (1.13 N-m) torque limit; and 3) the thermal-mechanical strains in a full assembly unit. Fig. 8 shows a measured multi-material interface area before and after speckle coated. Fig. 9 shows some typical strain patterns.

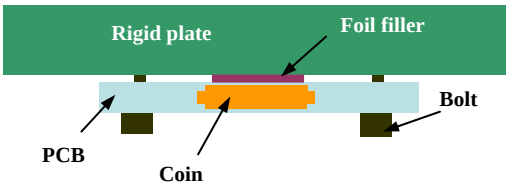

Fig. 7 A sketch of an assembly test sample.

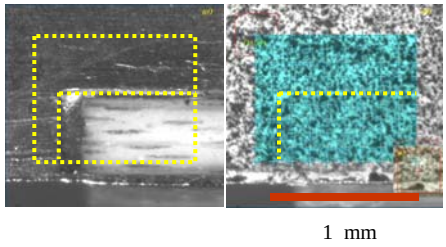

Fig. 8 The site measured using DSC before (left) and after (right) speckles coated.

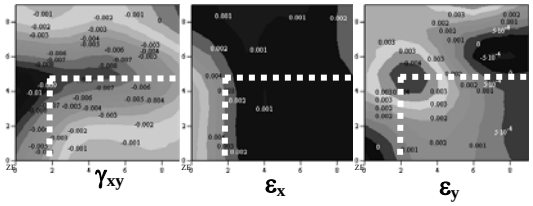

Fig. 9(a) Mechanical strains due to heat sink attachment with 0.006" thick TIM in local area as seen in Fig. 8.

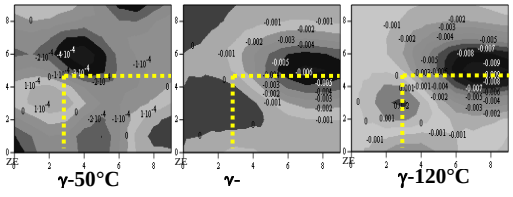

Fig. 9 (b) Thermal-mechanical shear strains at different temperatures in local area as seen in Fig. 8.

Fig. 9(a) and 9(b) give the area distribution of three in-plane mechanical strain and the shear strain at different elevated temperatures, respectively. The post-test visual inspection revealed that the thermally induced cracks were located exclusively along the horizontal interfaces between the tab locks and the PCB, as the photo in Fig. 10 typically shown. In measuring the thermal-mechanical strains, each test ended with a series of images recorded at various temperatures. Fig 10 summarizes the highest shear strain in the interconnect area. The data include 1) the mechanical strain due to heat sink attachment with the shim layer thickness of 3-mil and 6-mil, respectively; 2) the thermal-mechanical strain variation with temperature in PCB with the heat sink (but no PA) installed using fillers of 3-mil and 6-mil thickness; and 3) the thermal-mechanical strain in a full assembly package. The determination of the temperature/time that the fracture initiated was based on the strain release. As shown in Fig. 11, a significant strain drop is detected at 117 ^{o}C in the assembly package during the first test (with a 3 mil thick TIM insertion), which signifies the crack initiation. The strain release is confirmed in the second test in which a 6 mil thick TIM layer was used. Yet much lower strain was obtained in the same location. Given that the thicker TIM normally induces higher interface strain, the observed strain abnormality confirms that the crack existed prior to the second test. Therefore, 117 ^{o}C is considered as a captured critical failure temperature. The corresponding debonding strain of

around 0.012 is determined by adding the assembly induced mechanical strain at room temperature to the thermal-mechanical strain at 117 ^{o}C. The shear strain at 150 ^{o}C in the same area in a bare PCB is only about 0.003, also given in Fig. 10. By comparing the thermal-mechanical strains in the PCB-coin interface area between the bare PCB and the assembly, the study concludes that the full assembly package experiences a thermal-mechanical strain four times as high as that in a bare PCB. The conclusion quantitatively explains why the shock test (run at 150 ^{o}C extreme) on a bare PCB had produced no fracture failure.

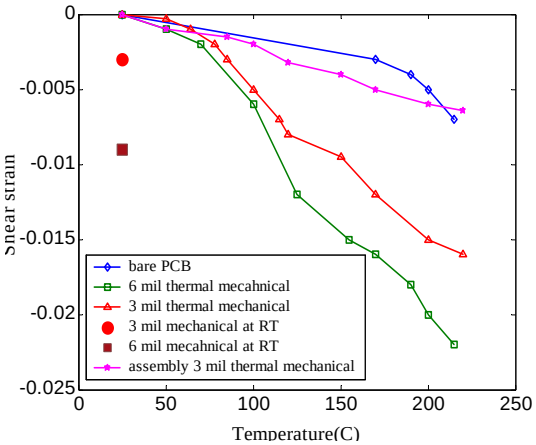

Fig. 10 Comparisons of shear strains in same vertical interface area measured from samples under different conditions. No crack was found. The samples include a bare PCB, a PCB and heat sink assembly (no PA) with different shim thickness, and a full PCB assembly with both PA and heat sink attached.

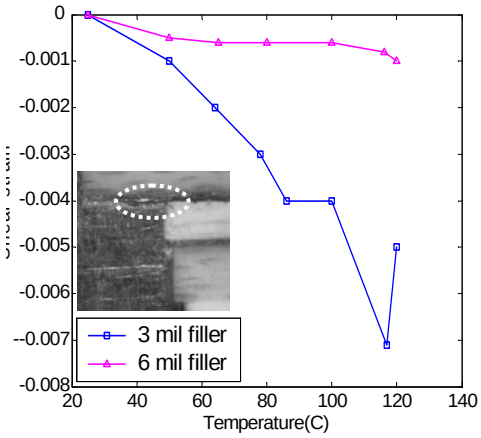

Fig.11 Failure analysis for a PCB sample based on strain measurement and visual inspection. Crack in a horizontal interface was determined to have occurred at 117°C with 3 mil filler.

3.2 Evaluation of mechanical reliability of large body BGA assembly

The 55 x 55 mm flip chip BGA (ball grid array) module has a 1 mm pitch full array of 2809 solder balls. The metal lid is a key element facilitating the heat dissipation. The module's extraordinary weight and size render the assembly susceptible to bending induced interconnect fracture. The conventional bend test for assessing mechanical reliability [4] of Sn-Pb soldered packages uses special Daisy chained samples. The material damage in the looped solder balls and routings are detected by monitoring the loop resistance increase. Yet for leadfree SAC (Sn-Ag-Cu) soldered packages, due to the high stiffness and strength of SAC, the interconnect cracking due to bending happens in the PCB underneath the copper-pad. The failure is typically referred to as "pad-cratering" [5]. Since the daisy chain has no response to the fracture in plastics, the standard bend test is no longer effective in assessing leadfree packages. A proposed method [5] uses the electric strain gauges on the module substrate to detect the substrate strain response to interconnect cracking. The method, however, encounters a serious challenge for the popular BGA packages with thermal lid. The lid prevents the strain gauges from laying on the substrate, unless a portion of it is removed [6].

The present study uses the FBG strain sensor to provide a needed solution. The test system is as the photo in Fig. 12 shows, which consists of a universal loading machine of 5000 lbs (22.3 KN) capacity equipped with four-point bend fixtures, a 10 KHz data acquisition system of 36 channel and 16 bit A/D converters, and an optical spectrum analyzer of the maximum sweep rate of 250/2000Hz. Two desktop computers provide interfaces for system control, parameter setting, data storage and real-time graphical display. The loading symmetry is monitored using a pair of LVDT (Linear Variable Differential Transformer) displacement transducers placed on the loading fixture and a pair of strain gauges on the PCB. Table 1 lists the test parameters. With a diameter of 0.25 mm, the sensor can fit to the narrow space along the substrate edges. Although the FBG sensor has high strain sensitivity, to capture the pad-cratering induced substrate response depends also on where the sensors are laid. The optimal locations are those close to where the first interconnect fail occurs. In this study, they were identified via the dye and pry test analysis and the microscopic visual inspection in combination with a three-dimensional FE modeling. Such a linear elastic model effectively indicates, as shown in Fig. 13, that the highly localized stress/strain in the PCB exists near the module's corners, where the visual inspection also concluded the occurrence of the first fail of solder joints. Furthermore, the FE results reveal the highest strain in the substrate exists along the substrate edges.

Fig. 12 4-point bend test system showing that the FBG strain sensing unit (the black box) connected with test sample with optical fibers .

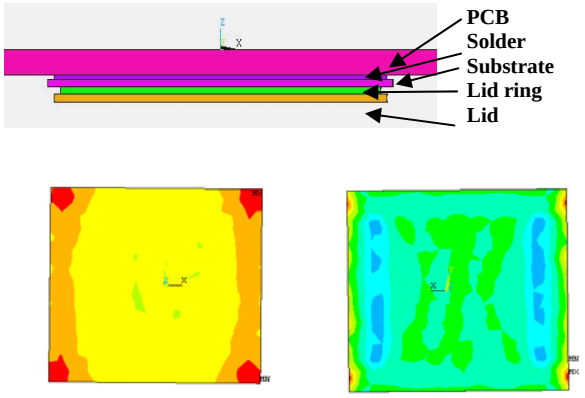

Fig. 13 FE structure model of an assembly package (top); solder layer shear strain distribution (bottom left); and substrate normal strain (bottom right).

The FE results were used in guiding the placement of the FBG sensors near the module corners. As Fig. 14 and 15 illustrate, the sensors are aligned in parallel with the substrate edges at a distance of 1.0 mm from the peripheral row of the solder balls. To enhance the sensitivity of event capturing, the sensors were made with 4 mm gauge/grating length. The end of the sensor grating was aligned to coincide with the corner ball, so that the grating length was extended to the fourth ball in the row. In the test, the substrate strain normally increases with the global

load increase. As the damage starts to happen in the nearby interconnects, the substrate strain variation is also affected. Fig. 16 shows typical variations with the time of the load, the PCB strain and the substrate corner strain. The strain release as seen happens before the global load and PCB strain reach their peaks. The differences among the four FBG strain curves may have been contributed by the slight asymmetry of the load and the interconnect strength. The strain fluctuation is attributed to the level of damage to the joint connectivity in the sensor areas. Similar phenomenon has been reported in the previous studies of microelectronic packages and thin films [7, 8, 9].

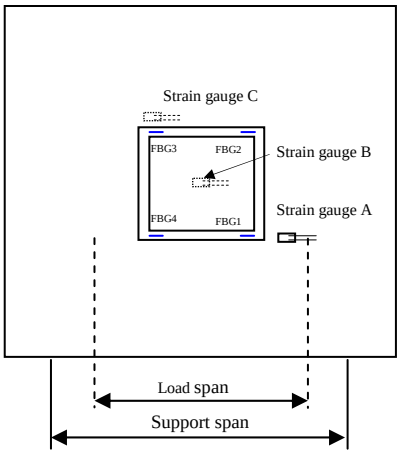

Fig. 14 Locations of FBG and strain gauges.

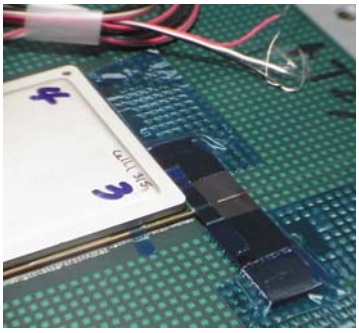

Fig. 15 Installation of FBG on corners of BGA substrate.

Table 1 Test setup parameters

Load span (mm)	Support span (mm)	Crosshead speed (mm/s)	Crosshead travel distance (mm)	Strain rate input (με/s)	Frequency of data collection (Hz)	Resistance of PCBA (Ω)	Current (A)
115	147	8.4	2-6	10000-14000	2000	9-12	0.2

Since the bending is directly applied to the PCB, the module shares a portion of the load that is transferred from the PCB via the solder joints. If a corner joint breaks, the load share in the substrate will redistribute to shift some away from the sensor area as manifested by a strain reduction in that area. On the contrary, if a joint beyond the corner/sensor's immediate proximity fails, the fracture will cause a shift of the load from the cracked area to the corner, inducing an increase of the sensor's strain. The stress redistribution in the substrate as the consequence of the interconnect fracture is captured by the FBG sensor and recorded with a time sequence. Based on the recorded strain variation, one may be able to distinguish the fractures occur in different locations and their sequence of occurrence. For instance, a sharp strain drop signifies a crack initiates right beside the sensor, while a steep spike exhibited in the strain curve represents the

sensor's response to a fracture that occurs somewhere away from the sensor's immediate proximity. The signature behavior of the abrupt hikes and drops manifest the onset of the brittle fracture of the interconnects, which is typical for the assemblies with 2 mm thick lid due to the so-enhanced module stiffness. The abrupt strain change in Fig 16(a) is usually transitory and occurs before the global board deflection or the load reaches the pre-defined maximum. As the global load further increases, the strain resumes the climbing trend indicating the localized nature of the captured fracture initiation. On the other hand, a slow but steady strain variation shown in Fig. 16(b) happens for a package with a 0.5mm thick lid. The slope of the strain curve reduces steadily indicating that a relatively larger area near the sensor is experiencing a continued but slow reduction of the load share, which is an evidence of the ductile type of interconnect fracture that develops gradually and simultaneously. The curve in Fig 16(b) shows no zigzag, but a monotonic, general "yielding" type of magnitude drop seen in the later stage of the loading. This indicates that the development of the fracture causes an accelerated strain reduction. Since the interconnect failure occurs in a larger area, the sensor strain cannot be sufficiently compensated by the global load increase. While the brittle fracture induces strain zigzags to mark the critical points on the strain curve in Fig. 16(a), there are no such points can be readily identified on a ductile fractured strain curve to pinpoint the critical failure instance.

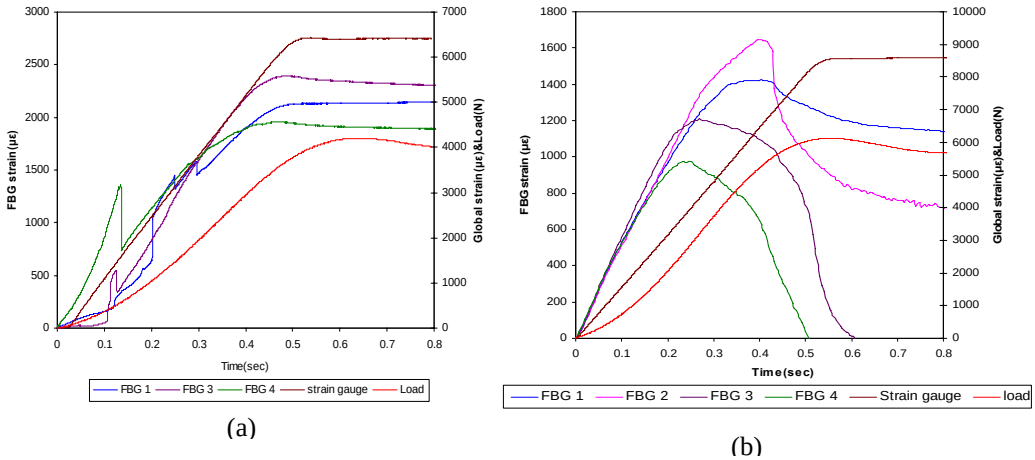

Figure 16 (a): FBG measured substrate corner strains showing spikes and drops in sample type a, indicating the occurrence of brittle interconnect fractures; and (b): smooth strain release for sample type b, representing ductile fractures.

4. Conclusions

Albeit the high cost and prolonged testing period, the statistics based failure tests dominate the standard reliability evaluation. One reason is that the physics-based failure analysis and life prediction become subtle in dealing with miniatures of a multiple material system, that is subject to various and variable conditions. A great majority of the interconnect materials show strong time and temperature dependent thermal and mechanical properties. The modes and mechanisms of the

package failures are versatile, varying with the package design, manufacturing and operation. With the coupled fracture, creep and fatigue failures, the packages' damage development is a complex process to model whether or not the existing theories are valid for materials in the micron and sub-micron scales. The applications presented in this paper have demonstrated that as the modeling of actual mechanisms for failure prediction is technically challenging, to pursue alternative experimental mechanics based approach seems to be a logical choice. Comparing with the current test regime that relies on lengthy and costly failure statistics based testing, the experimental mechanics-based measurement assisted by the physics-based modeling can provide a time and cost effective alternative.

5. Acknowledgements

The work has been partially sponsored by CMAP (Center for Microelectronic Assembly and Packaging) of Ontario. The collaboration with the researchers from the sponsor companies of Motorola, Celestica and IBM is acknowledged and greatly appreciated.

6. References

1. Hua Lu, "Application of Digital Speckle Correlation to Microscopic Strain Measurement and Materials' Property Characterization", *Transaction of the ASME Journal of Electronic Packaging,* Vol. 120, September 1998, pp. 275-279.

2. Kersey A.D., Davis M.A., Patrick H.J, LeBlanc M., Koo K. P., Askins C.G, Putnam M.A., Friebele E.J., "Fiber grating sensors", IEEE Trans. Rel., vol. 15, issue 8, pp.1442-1463, Aug. 1997.

3. V. Chiriac and T. Lee, 2004, Thermal Evaluation of Power Amplifier Modules and RF Packages in a Handheld Communicator System, 2004 Inter Society Conference on Thermal Phenomena pp 557-563.

4. Lei L. Mercado, George Hsieh, and Steven Girouard, "Electronic Packaging Solder Joint Reliability Assessment with a Mechanics-Based Strain Gage Methodology," IEEE Trans. \Rel., vol. 29, no1, pp.5-12, Mar. 2006.

5. Jason Bragg, Adam Zbrzezny, Albert Lai, Suthakaran Subramaniam, George Riccitelli and Heather McCormick, "Bend and Drop Testing Results for a Leadfree and Tinlead 45 mm Flip Chip BGA", Proceedings of SMTA conference, Toronto, 2007.

6. George Hsieh, Alan Mcallister, "Flip chip ball array component testing under board flexure", Electronic Components and Technology Conference, pp937-944, 2005.

7. Thomas Koschmieder, "Experiences with monotonic bend test of electronic packages," SMTA conference proceedings, pp 406-411, Nov, 2007.

8. R. Shaviv, S. Roham, P. Woytowitz, "Optimizing the precision of the four-point bend test for the measurement of thin film adhesion," Microelectronic Engineering 82 (2005) pp. 99–112.

9 R. Shaviv, S. Roham, P. Woytowitz, "Optimizing the precision of the four-point bend test for the measurement of thin film adhesion," Microelectronic Engineering 82 (2005) pp. 99–112.